expression in *Escherichia coli* as described by X. Liao, K. R. Clemens, J. Cavanagh, L. Tennant, and P. E. Wright [*J. Biomol. NMR* **4**, 433 (1994)]. We performed the NMR experiments at 300 K at a ^{1}H frequency of 500 MHz, using a 0.5 mM solution of ZF1–3 in 30 mM phosphate buffer (pH 6.5) in a mixture of 90% H_2O and 10% D_2O containing 30 mM NaCl, 5 mM deuterated dithiothreitol, and 50 μM $ZnCl_2$.

7. Analysis of the data, accounting for both dipolar relaxation of the ^{15}N spin mediated by its directly attached proton and relaxation caused by chemical shielding anisotropy, was based on the classical expressions (8)

$$T_1^{-1} = \sum_j a_j J(\omega_j)$$

$$T_2^{-1} = \sum_j b_j J(\omega_j)$$

$$\eta = 1 + \frac{\omega_H}{\omega_N} T_1 \sum_j c_j J(\omega_j)$$

with constant coefficients a_j, b_j, and c_j. The power spectral density $J(\omega)$ reflects molecular dynamics processes (intramolecular dynamics as well as overall rotational tumbling) and is sampled at frequencies ω_j, which are combinations of the ^{15}N and ^{1}H Larmor frequencies ω_N and ω_H.

8. L. E. Kay, D. A. Torchia, A. Bax, *Biochemistry* **28**, 8972 (1989).

9. M. J. Stone *et al.*, *ibid.* **31**, 4394 (1992).

10. P. Debye, *Polar Molecules* (Dover, New York, 1929), chap. 5; F. Perrin, *J. Phys. Radium* **5**, 497 (1934); *ibid.* **7**, 1 (1936); L. D. Favro, *Phys. Rev.* **107**, 7 (1960).

11. G. Lipari and A. Szabo, *J. Am. Chem. Soc.* **104**, 4546 (1982).

12. W. H. Press, B. P. Flannery, S. A. Teukolsky, W. T. Vetterling, *Numerical Recipes in C: The Art of Scientific Computing* (Cambridge Univ. Press, Cambridge, 1988).

13. Structures were calculated from 1284 NOE distance constraints and 45 dihedral angle constraints by variable target function distance geometry and restrained molecular dynamics (X. Liao and P. E. Wright, unpublished data).

14. M. S. Lee, G. P. Gippert, K. V. Soman, D. A. Case, P. E. Wright, *Science* **245**, 635 (1989); R. E. Klevit, J. R. Herriott, S. J. Horvath, *Proteins* **7**, 215 (1990).

15. Y. Nakaseko, D. Neuhaus, A. Klug, D. Rhodes, *J. Mol. Biol.* **228**, 619 (1992).

16. J. G. Omichinski *et al.*, *Biochemistry* **31**, 3907 (1992).

17. Contributions from aggregation can be excluded as a result of the excellent agreement found between the effective rotational tumbling correlation time obtained by tryptophan fluorescence depolarization measurements at a ZF1–3 concentration of 50 μM and that derived from NMR relaxation measurements at more than 10-fold higher concentration (X. Liao, R. Brüschweiler, D. Millar, P. E. Wright, unpublished data).

18. A. G. Palmer, M. Rance, P. E. Wright, *J. Am. Chem. Soc.* **113**, 4371 (1991).

19. G. Barbato, M. Ikura, L. E. Kay, R. W. Pastor, A. Bax, *Biochemistry* **31**, 5269 (1992).

20. It is not possible to specify uniquely the relative orientations of the diffusion tensors as a consequence of the transformation properties of the responsible spin interactions. The relaxation data cannot distinguish between orientations that relate individual domains by an orthorhombic symmetry transformation of the diffusion tensor ellipsoids. This means that a 180° rotation of any of the domains about the x, y, or z axes of their diffusion frames leaves the relaxation parameters unchanged.

21. I. Radhakrishnan, D. Millar, P. E. Wright, unpublished data.

22. K. R. Clemens *et al.*, *J. Mol. Biol.* **244**, 23 (1994).

23. We thank T. Macke for making Fig. 1 (with graphics program AVS) and D. Millar and J. Gottesfeld for helpful discussions. X.L. is a recipient of the Cancer Research Institute–Miriam and Benedict Wolf Fellowship. This work was funded by grant GM 36643 from the National Institutes of Health.

8 November 1994; accepted 21 February 1995

Borders of Multiple Visual Areas in Humans Revealed by Functional Magnetic Resonance Imaging

M. I. Sereno,* A. M. Dale, J. B. Reppas, K. K. Kwong, J. W. Belliveau, T. J. Brady, B. R. Rosen, R. B. H. Tootell

The borders of human visual areas V1, V2, VP, V3, and V4 were precisely and noninvasively determined. Functional magnetic resonance images were recorded during phase-encoded retinal stimulation. This volume data set was then sampled with a cortical surface reconstruction, making it possible to calculate the local visual field sign (mirror image versus non–mirror image representation). This method automatically and objectively outlines area borders because adjacent areas often have the opposite field sign. Cortical magnification factor curves for striate and extrastriate cortical areas were determined, which showed that human visual areas have a greater emphasis on the center-of-gaze than their counterparts in monkeys. Retinotopically organized visual areas in humans extend anteriorly to overlap several areas previously shown to be activated by written words.

Over half of the neocortex in nonhuman primates is occupied by visual areas. At least 25 visual areas beyond the primary visual cortex (V1) have been identified with a combination of microelectrode mapping, tracer injections, histological stains, and functional studies (1). The analysis of this data has been greatly aided by the use of flattened representations of the cortical surface made from conventional sections with graphical techniques (2) and flattened wire models (3), or more directly from sections of physically flat-mounted cortex (4).

A large portion of the neocortex in humans is likely to be occupied by visual areas too. It has been difficult, however, to outline unambiguously any human cortical area with noninvasive techniques. Previous studies have mapped only a few locations in the visual field or have relied on stimulus features to activate different areas (5), and the tortuous convolutions of the human neocortex have defied previous attempts to see activity across all of its surface area at once.

Many of the cortical visual areas in nonhuman primates are retinotopically organized to some degree (3, 6). These areas are irregularly shaped and somewhat variable in location; consequently, recordings from many locations (400 to 600) in single ani-

M. I. Sereno, Cognitive Science 0515, University of California, San Diego, La Jolla, CA 92093–0515, USA.
A. M. Dale, Cognitive Science 0515, University of California, San Diego, La Jolla, CA 92093–0515, USA, and Department of Neurophysiology, University of Oslo, 0316 Oslo, Norway.
J. B. Reppas, Harvard–Massachusetts Institute of Technology Division of Health Sciences and Technology, Boston, MA 02115, USA.
K. K. Kwong, J. W. Belliveau, T. J. Brady, B. R. Rosen, R. B. H. Tootell, Massachusetts General Hospital Nuclear Magnetic Resonance Center, 149 13th Street, Charlestown, MA 02129, USA.

*To whom correspondence should be addressed.

mals have been required to define areal borders with confidence (7). Here we demonstrate a technique for generating retinotopic maps of visual cortex in humans with a precision similar to that obtained in the most detailed invasive animal studies. Responses to phase-encoded retinal stimulation (8) were recorded with echo-planar functional magnetic resonance imaging (MRI) (9) and analyzed with a Fourier-based method. The resulting volume data sets were sampled with a cortical surface reconstruction made from high-resolution structural MRI images collected separately for each participant (10). The cortical surface containing the data was then unfolded and analyzed with the visual field sign method to distinguish mirror image from non–mirror image representations (7). By combining these four techniques (multislice functional MRI, stimulus phase-encoding and Fourier analysis, cortical surface reconstruction, and visual field sign calculations), it was possible to reconstruct the retinotopic organization of visual areas V1, V2, VP, V3, and V4 in humans in two dimensions and to accurately trace out the borders between these areas in the living human brain.

To map polar angle (angle from the center-of-gaze), we obtained 128 asymmetric spin echo MRI images (11) of 8 to 16 oblique sections perpendicular to the calcarine sulcus (1024 to 2048 total) in a 512-s session (~8.5 min) while participants (n = 7) viewed a slowly rotating (clockwise or counterclockwise), semicircular checkerboard stimulus. Eccentricity (distance from the center-of-gaze) was mapped with a thick ring (dilating or contracting) instead of a semicircle. These four kinds of stimuli elicit periodic excitation at the rotation or dilation-contraction frequency at each point in a cortical retinotopic map (8, 12). The

phase of the periodic response at the rotation or dilation-contraction frequency, measured with the (complex-valued) Fourier transform of the response profile over time at each voxel, is closely related to the polar angle or eccentricity represented at that cortical location (13). This technique results in high signal-to-noise ratios (because at any one point in time, approximately one-half of each visual field map will be activated) yet provides fine spatial resolution. Common (for example, retinal) and between-area phase delays can be removed and examined by considering clockwise-counterclockwise rotation and expansion-contraction pairs (14, 15).

Figure 1A shows a color plot of the response to a dilating ring on a medial view of the cortical surface of the brain of this participant (A.M.D.) (16). The hue of the color at each cortical surface point indicates the response phase, which is here proportional to the eccentricity of the local visual field representation. In Fig. 1B the cortical surface was unfolded. This process is similar to inflating a crumpled balloon except that the surface has not been stretched. In Fig. 1C, the occipital lobe region containing the activated area has been cut off and the resulting approximately conical surface cut again along the fundus of the calcarine sulcus to allow it to be flattened completely (17).

There is a systematic increase in eccentricity (red to blue to green to yellow to red) moving anteriorly along the medial wall of the occipital cortex. Lines of isoeccentricity run approximately in the coronal plane, cutting across several areas, as shown below. Ventrally, the region showing substantial retinotopy extends almost to the anterior-posterior midpoint of the unfolded ventral temporal lobe.

A parallel treatment of data from the rotating hemifield stimulus collected a few minutes later is shown in Fig. 1, D and E. The color again indicates the phase of the periodic response, which is now proportional to the polar angle of the local visual field representation. The picture of polar angle is more complex, alternating between vertical and horizontal meridians both dorsally and ventrally. The upper field vertical meridian is red, the horizontal meridian is blue, and the lower field vertical meridian is green. Several alternations between red and blue stripes are visible ventrally, whereas several alternations between green and blue stripes are visible dorsally. Mapping experiments in monkeys suggest that several additional rerepresentations of the lower visual field adjoin V1 dorsally, including V2 (second visual area) and V3 (third visual area), whereas several rerepresentations of the upper visual field adjoin V1 ventrally, including V2, VP (ventroposterior area), and V4v

(V4 ventral) (18). In particular, we would expect vertical meridian representations at the dorsal and ventral V1-V2 border, the ventral VP-V4v border, and the dorsal V3-V4 border, and horizontal meridian representations near the fundus of the calcarine sulcus in V1, at the dorsal V2-V3 border, at the ventral V2-VP border, and at the anterior border of ventral V4v (4, 6, 7). Candidates for all of the borders are visible in
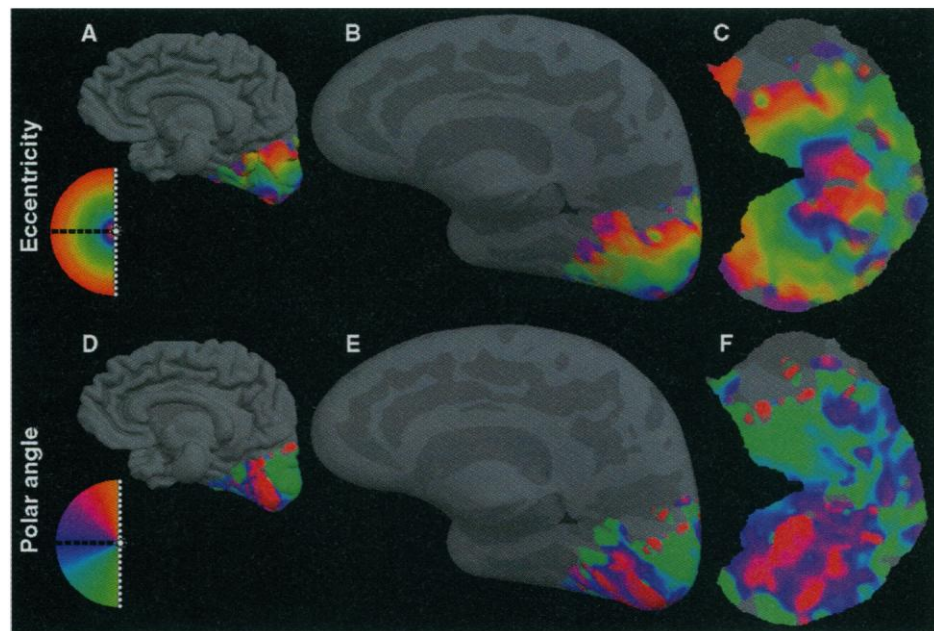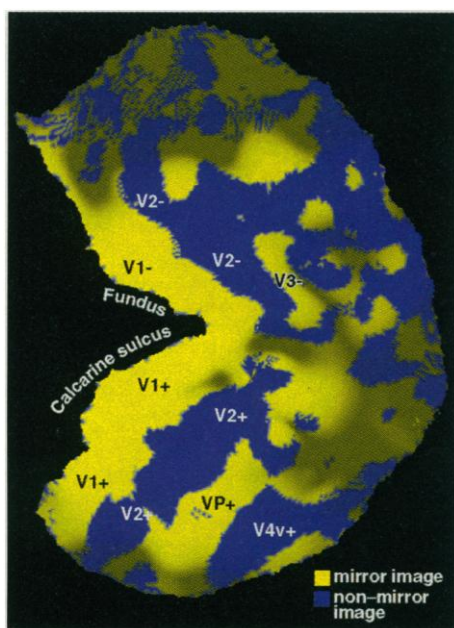

Fig. 1. Isoeccentricity and isopolar angle maps of human visual areas. The top row shows isoeccentricity coded by color [red (fovea) → blue → green (parafoveal) → yellow → red (periphery)] displayed on the original cortical surface (**A**), the unfolded cortical surface (**B**), and the cut and flattened cortical surface (**C**). The bottom row shows polar angle [red (lower vertical meridian) → blue (horizontal meridian) → green (upper vertical meridian)] plotted on the same three surfaces (**D**), (**E**), and (**F**), respectively. Local eccentricity and polar angle were determined by considering the phase of the response to a slowly dilating ring or a slowly rotating hemifield at the dilation or rotation frequency. The unfolded representations in (B) and (E) were made by relaxing the curvature while approximately preserving local area and local angles (the sulcal cortex is dark gray and the gyral cortex light gray). The flattened representations in (C) and (F) were made with the same algorithm after the occipital lobe was cut off and an additional cut in the fundus of the calcarine sulcus was made.
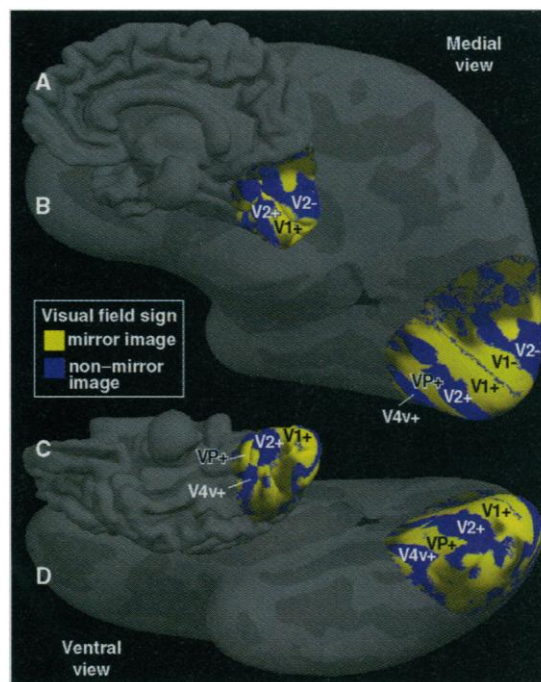
Fig. 2. Analysis of the data in Fig. 1 by visual field sign (mirror image versus non–mirror image visual field representation). Mirror image areas (yellow; for example, V1), and non–mirror image areas (blue; for example, V2) are shown in a medial view on the folded (**A**) and unfolded surface (**B**) and in a ventral view, folded (**C**) and unfolded (**D**). The incision in the fundus of the calcarine is visible in (B). Ventral V1, V2, VP, and V4v (18), comprising four rerepresentations of the upper visual field, are visible below the incision, whereas lower visual field V1 and V2 are visible above the incision. The complex folding pattern of the occipital lobe coupled with the weak correlation between sulci and areal boundaries underscores the need for an unfolded representation.

Fig. 1, D and E. Mapping experiments in monkeys have also revealed a number of small visual areas beyond those mentioned so far (including the parietal-occipital area), which may help to explain the presence of several small patches of lower field dorsally as well as upper field ventrally.

Isoeccentricity and isopolar angle maps define two independent coordinates of retinotopy. Areal borders in either one of these maps, however, are often subtle; isoeccentricity lines can extend straight across several areas, whereas polar angle maps often show only a shallow maximum or minimum at the border of an area. For example, the red stripe at the ventral upper field vertical meridian border of V1-V2 actually extends across both V1 and V2. In contrast, the visual field sign technique (7) provides an objective means to draw borders between areas on the basis of an analysis of the local relation between the directions of the fastest rate of change in these two coordinates. Regions of the cortex that contain a retinotopic map, however distorted, can be divided into two categories when viewed from the cortical surface: those that contain a mirror image representation of the visual field (like V1) and those that contain a non–mirror image representation of the visual field (like V2). This distinction is un-

likely to be of any fundamental functional significance, but it provides a convenient way to draw borders between areas because adjoining areas often have the opposite visual field sign. It is a local measure that can be calculated for each small patch of cortex given dense retinotopic mapping data like those obtained here.

A map of visual field sign is shown on the folded and unfolded surface in a medial view (Fig. 2, A and B) and in a ventral view (Fig. 2, C and D) (19). V1 is now clearly outlined as a large mirror image patch (yellow) divided by our incision at the fundus of the calcarine sulcus. V2 forms two non–mirror image patches (blue) dorsally and ventrally. Two more areas are visible ventral and anterior to ventral V2: mirror image VP (yellow) and, finally, non–mirror image V4v (blue).

In Fig. 3, the cortex has been completely flattened, exposing the dorsal and lateral areas concealed in Fig. 2. Dorsal V2 is adjoined anteriorly by a thin band of mirror image V3 (yellow). Just ventral and anterior to V3 the visual field sign pattern degenerates into noise near the center-of-gaze representations of V1 and V2, likely the result of the difficulty of mapping foveal cortex

with this technique (20). Dorsal and anterior to V3 there are additional non–mirror image areas (blue) containing both upper and lower visual field representations that may correspond in part to V3A (V3 accessory) and dorsal V4 (not labeled). Even further anteriorly, areas are less obviously modulated at the stimulus rotation or dilation-contraction frequency, indicating that they are either foveal (<0.5°), peripheral (>12°), or less well organized retinotopically. Similar results were obtained from six other individuals.

The areas revealed in these experiments show a number of similarities to areas originally discovered in nonhuman primates. A schematic comparison of the human visual areas with macaque monkey visual areas (21) and owl monkey visual areas (7) is shown in Fig. 4. At the top, the three flattened cortices are drawn at the same absolute scale, whereas at the bottom, they are approximately scaled by the area of V1. It has long been known that V1 in humans is shifted medially around the occipital pole when compared with the location of V1 in monkeys. The larger size of some human extrastriate areas relative to human V1 may have partially compensated for this shift

Fig. 3. Visual field sign displayed on the completely flattened occipital cortex (brightness indicates significance of the response). Upper visual field V1, V2, VP, and V4v and lower visual field V1, V2, and V3 are now all visible. There are several robustly responding non–mirror image regions anterior to dorsal V2 and V3 that may correspond in part to V3A and dorsal V4 (not labeled). Regions with dimmer coloration may represent the central fovea (20) or the visual field beyond 12° eccentricity, or they may be less retinotopic.

Fig. 4. Schematic summary of retinotopic visual areas in the owl monkey (7), the macaque monkey (21), and the human (present study) at the same scale (**A**) and approximately normalized by the area of V1 (**B**). (Human V1 is twice the area of macaque V1, with larger ocular dominance columns and cytochrome oxidase blobs, but a similar number of cells.) Visual areas in humans show a close resemblance to visual areas originally defined in monkeys. The anterior border of the visual cortex in humans was estimated by using the superior temporal sulcus and intraparietal sulcus as landmarks. In (**C**), the mapping functions (heavy lines; scale is on the left axis) and magnification factor functions (light lines; scale is on the right axis) are shown for the upper field representations of human V1, V2, VP, and V4 (24). The V1 mapping functions for owl monkeys (OM*, dotted) and macaque monkeys (MM*, dashed) shown at the left were scaled up to match the overall size of human V1 (25). An increased emphasis on the center-of-gaze in human V1 is evident. CMF, cortical magnification factor.

891
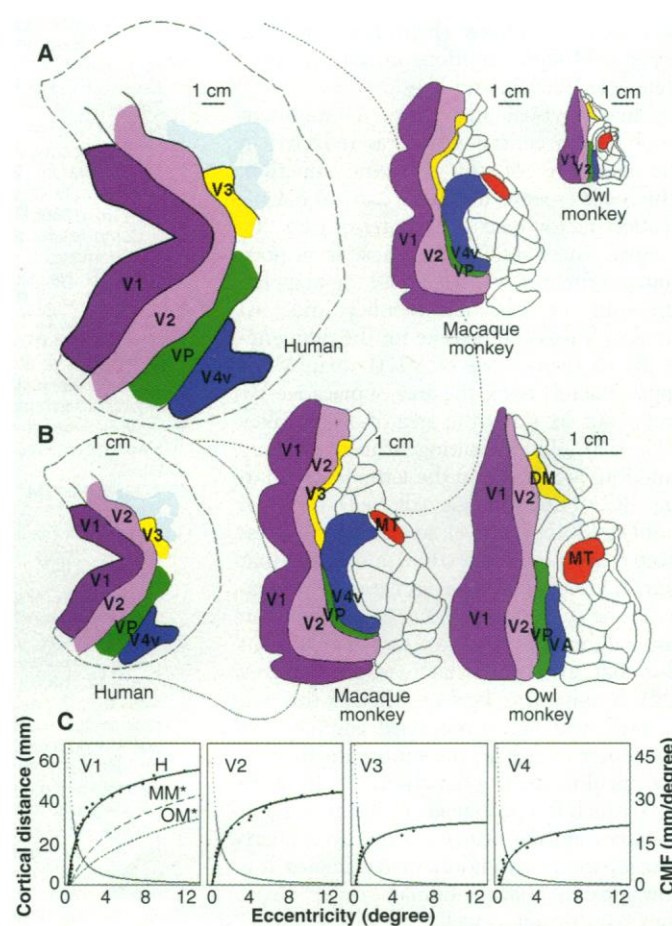
[see for example the width of VP in Fig. 4B and the region between V2 and MT in (22)]; retinotopic areas extend nearly to the anterior-posterior midpoint of the ventral temporal lobe, just as they do in nonhuman primates. The anterior extent of retinotopic visual areas is most striking in the unfolded ventral view (Fig. 3D). Comparisons with the folded ventral view (Fig. 3C) show that more cortex is hidden in the posterior folds of the ventral occipital lobe than in the more anterior ventral temporal fissures.

The internal structure of a visual cortical map can be characterized with the linear cortical magnification factor, $M(r)$, millimeters of cortex per degree of visual angle as a function of eccentricity, r (23). We estimated the value of the parameters in a standard equation for magnification factor by measuring eccentricity on the cortical surface parallel to the average direction of fastest change of eccentricity in each upper and lower visual field representation described above. The resulting measurements were fit with a cortical mapping function, $D(r)$ [the distance on the cortex as a function of eccentricity (the integral of the magnification factor equation)] by adjusting the parameters (24). Figure 4C shows the data and estimated mapping functions (points and heavy lines) and corresponding cortical magnification factor functions (light lines) for the upper field representations in human visual areas V1, V2, VP, and V4v.

Human visual areas show a prominent emphasis on central vision, as reflected in the steepness of the mapping function, which corresponds to a large cortical magnification factor near the center-of-gaze. To compare these results with those from nonhuman primates, we first scaled the mapping functions for macaque monkey and owl monkey V1 to compensate for the differences in the overall size of V1 (human V1 is approximately twice the area of macaque V1 and about six times the area of owl monkey V1) (25). The resulting scaled mapping functions are shown in the leftmost graph in Fig. 4C. The macaque (dashed) and owl monkey (dotted) curves are considerably less steep than the human curve, indicating that human visual areas have an extreme emphasis on the center-of-gaze, surpassing that seen not only in the nocturnal owl monkey but also that in the diurnal macaque monkey (26). It remains to be seen whether this will be explained by an increased emphasis on the center-of-gaze in the retina, in the retinogeniculocortical projection, or in both (27). Much has been made of the changes in areas beyond the primary cortex in humans in comparison with nonhuman primates. It is now apparent that the human primary visual cortex is distinct as well.

These studies of retinotopy in humans provide a framework for understanding the results of experiments designed to examine cortical responses to more complex and meaningful stimuli such as pictures, words, scenes, and sentences. It is interesting to note that several of the foci identified in previous noninvasive and invasive studies of responses to complex stimuli such as words (28) may overlap retinotopically organized areas already known from nonhuman primates. The techniques used here could be adapted to map tonotopy and amplitopy in the auditory cortex and somatotopy in the somatosensory cortex.

REFERENCES AND NOTES

1. M. I. Sereno and J. M. Allman, in *The Neural Basis of Visual Function*, A. G. Leventhal, Ed. (Macmillan, London, 1991), pp. 160–172; J. H. Kaas and L. A. Krubitzer, *Neuroanatomy of Visual Pathways and their Retinotopic Organization*, B. Dreher and S. R. Robinson, Eds. (Macmillan, London, 1991), pp. 302–359; D. J. Felleman and D. C. Van Essen, *Cereb. Cortex* **1**, 1 (1991); M. G. P. Rosa, J. G. Soares, M. Fiorani Jr., R. Gattass, *Visual Neurosci.* **10**, 827 (1993).
2. D. C. Van Essen and S. M. Zeki, *J. Physiol. (London)* **277**, 193 (1978); D. C. Van Essen and J. H. Maunsell, *J. Comp. Neurol.* **191**, 255 (1980).
3. R. Gattass, A. P. B. Sousa, C. G. Gross, *J. Neurosci.* **8**, 1831 (1988).
4. R. B. Tootell, M. S. Silverman, R. L. De Valois, *Science* **214**, 813 (1981); C. G. Cusick, H. J. Gould, J. H. Kaas, *J. Comp. Neurol.* **230**, 311 (1984); R. B. H. Tootell, S. L. Hamilton, M. S. Silverman, *J. Neurosci.* **5**, 2786 (1985); J. Olavarria and R. C. Van Sluyters, *J. Neurosci. Methods* **15**, 191 (1985); L. A. Krubitzer and J. H. Kaas, *Visual Neurosci.* **5**, 165 (1990).
5. P. T. Fox, F. M. Miezin, J. M. Allman, D. C. Van Essen, M. E. Raichle, *J. Neurosci.* **7**, 913 (1987); S. Zeki *et al.*, *ibid.* **11**, 641 (1991); W. Schneider, D. C. Noll, J. D. Cohen, *Nature* **365**, 150 (1993).
6. W. T. Newsome, J. H. R. Maunsell, D. C. Van Essen, *J. Comp. Neurol.* **252**, 129 (1986); D. J. Felleman, J. J. Knierim, D. C. Van Essen, *Soc. Neurosci. Abstr.* **12**, 1182 (1986); R. Desimone and L. G. Ungerleider, *J. Comp. Neurol.* **248**, 164 (1986); D. R. Boussaoud, R. Desimone, L. G. Ungerleider, *ibid.* **306**, 554 (1991); S. Neuenschwander, R. Gattass, A. P. B. Sousa, M. C. G. P. Piñon, *ibid.* **340**, 65 (1994).
7. M. I. Sereno, C. T. McDonald, J. M. Allman, *Cereb. Cortex* **4**, 601 (1994); *Cereb. Cortex*, in press.
8. S. A. Engel *et al.*, *Nature* **369**, 525 (1994); E. A. DeYoe, P. Bandettini, J. Neitz, D. Miller, P. Winans, *J. Neurosci. Methods* **54**, 171 (1994).
9. J. W. Belliveau *et al.*, *Science* **254**, 716 (1991); K. K. Kwong *et al.*, *Proc. Natl. Acad. Sci. U.S.A.* **89**, 5675 (1992).
10. A. M. Dale and M. I. Sereno, *J. Cog. Neurosci.* **5**, 162 (1993).
11. Echo-planar images were collected on a 1.5-T scanner (GE Signa) with full-body gradient coils (Advanced NMR) by using an asymmetric spin echo sequence [$\Delta\tau$ (offset time) = −25 ms, TE (echo time) = 70 ms, TR (repetition time) = 3000 to 4000 ms] [G. L. Wismer *et al.*, *J. Comp. Assist. Tomogr.* **12**, 259 (1988); J. R. Baker *et al.*, *Proc. Soc. Mag. Reson. Med.*, **12**, 1400 (1993); R. B. H. Tootell *et al.*, *J. Neurosci.*, in press]. A 5-inch receive-only surface radio frequency (RF) coil or a receive-only wrap RF coil was positioned near the occipital pole. Eight to 16 contiguous oblique 4-mm slices (voxel size: 3 mm by 3 mm by 4 mm) were chosen to lie approximately perpendicular to the calcarine sulcus. Before and after the set of functional scans for a participant, we recorded a T1-weighted series of echo-planar images [spin echo inversion recovery sequence: TE = 40 ms, TI (inversion time) = 1050 ms, TR = 20,000 ms, NEX (number of excitations) = 2] with the same orientation, slice thickness, and field of view as the functional scans. We used the T1 series to align the functional scans with the higher resolution structural

scan (voxel size: 1 mm by 1 mm by 1 mm) used for surface reconstruction that were collected in a separate session with a head coil.
12. The visual stimuli were generated in real time on a Silicon Graphics Onyx computer with GL graphics library functions. The high-resolution red green blue (RGB) video output signal was subsampled and converted to a composite video signal that was used to drive a Sony 2000 color liquid crystal display (LCD) projector. Informed consent to these experiments was obtained from the participants, several of whom were also authors (M.I.S., A.M.D., R.B.H.T.). Supine participants looked up into an adjustable angled mirror that allowed them to comfortably view a frosted back-projection screen arranged perpendicular to the bore just below their chin. Residual head movements were controlled through the use of a dental impression bite bar made before the scan for each participant and supported by an adjustable plastic yoke. Care was taken to block the participant's direct view of the screen. Participants were given the opportunity to take ibuprofen (200 to 600 mg) before the scan as a prophylactic against the minor discomforts that typically accompany attempts to remain very still for extended periods of time. Images were projected onto the screen through a collimating lens and subtended a maximum visual angle 35° wide and 26° tall. Stimuli consisted of black and white checkerboard patterns counterphase flickering at 4 Hz (that is, one cycle consists of 1/8 s of black and 1/8 s of white), which is near the optimal temporal frequency for driving cortical neurons [(5); K. H. Foster, J. P. Gaska, M. Nagler, D. A. Pollen, *J. Physiol.* **365**, 331 (1985)]. The checkerboard patterns were scaled with eccentricity. These patterns stimulated a circle in the visual field with a radius of 10° to 13°. The ring and hemifield stimuli were designed to activate approximately half of the ganglion cells in the central 10° to 13° of the two retinae at any one point in time.
13. The time series of activation (across the 128 images of each slice) was examined on a pixel-by-pixel basis. The linear trend and baseline offset for each pixel time series was first removed by subtracting off a line fitted through the data by least squares. The discrete Fourier transform of the time series for each pixel was then computed to give 128 complex values. In retinotopically organized areas, the amplitude spectrum showed a sharp peak at the stimulus rotation or dilation-contraction frequency (~0.015 Hz) 5 to 30 times as large as the peaks at other frequencies. The phase angle of the response at the stimulus rotation (or dilation-contraction) frequency at a voxel is related to the polar angle (or eccentricity) represented there. The phase angles for the pixels in a slice were then corrected to take account of delays resulting from the known order in which the slices were collected (1, 3, 5. . .2, 4, 6. . .). Finally, the phase angles were mapped to different hues whose intensity was a function of the ratio between the amplitude at the stimulus frequency and the average amplitude of all other frequencies (this ratio can reach 25 to 30 in V1). Our basic procedure is closely related to correlation of the signal with a sinusoid [compare P. A. Bandettini *et al.*, *Magn. Reson. Med.* **25**, 390 (1992); P. A. Bandettini, A. Jesmanowicz, E. C. Wong, J. S. Hyde, *ibid.* **30**, 161 (1993)].
14. In general, the phase of the periodic response will be delayed because of a finite vascular response time. The basic stimulus frequency was low enough so that there was no whole-cycle phase ambiguity. Residual phase delays were canceled by considering the circular average of the phase angles obtained for opposite directions of stimulus motion (contraction versus expansion, clockwise versus counterclockwise) at each voxel after the phase angles for the opposite stimulus direction were reflected around 0.
15. We rejected scans in which substantial movement (~2 mm) had occurred. This was easily recognized by viewing animations of the 128 images for each slice. Nevertheless, even in the presence of such movements, a sharp peak at the basic stimulus frequency (~0.015 Hz) was usually larger than the lower frequency peaks due to movement. Note that we have discretely sampled a continuous function: the intensity of a given voxel over time. Because that signal has not been explicitly limited in bandwidth

before sampling, there is also the danger that frequencies higher than the Nyquist critical frequency ($f_c \equiv 1/2\Delta \approx 0.12 - 0.25$ Hz for $TR = 2000$ to 4000 ms) could alias back into the spectrum we intended to measure. Changes in the signal due to blood oxygenation are unlikely to be fast enough to cause such a problem. Artifactual signals due to brain motion caused by rapid head motion were controlled through the use of a bite bar. Brain movement artifacts induced by cardiac pulsation are potentially more problematic; however, there is enough variation in frequency and phase of the cardiac signal to avoid the generation of large aliased peaks in the Fourier amplitude spectrum given the number of stimulus cycles used in the present study.

16. To paint the functional data onto the cortical surface, blink comparison in three orthogonal planes was first used to align the echo-planar inversion recovery images (3 mm by 3 mm by 4 mm, taken in the plane of the functional images) with the high-resolution data set (1 mm by 1 mm by 1 mm) used to reconstruct the cortical surface (17). The functional data set was then sampled with the cortical surface. By using a surface nearer to the gray-white matter border than to the pial surface, we were able to accurately assign activations to the correct bank of a sulcus despite the fact that the individual functional voxels were comparable in size to the thickness of the cortex. Our success in this endeavor is demonstrated by the lack of ambiguity in recovering the closely apposed upper and lower visual field representations situated on opposite sides of the calcarine sulcus. The lower resolution activation data (one sample $\cong$ 3 mm by 3 mm) was smoothly interpolated onto the high-resolution surface reconstruction (one polygon $\cong$ 1 mm by 1 mm).

17. The folded, unfolded, and flattened surfaces were made from high-resolution T1-weighted images (1 mm by 1 mm by 1 mm) optimized for gray-white matter contrast with techniques similar to those presented in (10) [compare E. L. Schwartz, in *Computational Neuroscience*, E. L. Schwartz, Ed. (Wiley, New York, 1990), pp. 295–315; and G. J. Carman, thesis, California Institute of Technology (1990)]. The skull was first automatically stripped off by "shrink-wrapping" a stiff deformable template onto the brain. The gray-white matter boundary for each hemisphere was then estimated with a region-growing method. The result was tessellated to generate a surface (~150,000 vertices) that was refined against the MRI data by using a deformable template algorithm, inspected for topological defects (for example, "handles"), and remade if necessary. It was unfolded by area-preserving curvature reduction. A completely flattened cortical surface was obtained by cutting off the occipital lobe and incising the fundus of the calcarine by disconnection of vertices. The resulting surface fragment was then pushed onto a coronal plane in one step and unfurled on the plane. The vertex update rule was modified from that in (10) to include both local area–preserving and shear-minimizing terms. Beautiful images of the cortical surface can be generated by rendering stacked slices [H. Damasio and R. Frank, *Arch. Neurol.* **49**, 137 (1992)]. Such images, however, lack explicit information about the cortical surface orientation and connectivity required for cortical unfolding. It is possible to trace the cortical ribbon in individual slices and manually connect them into a surface [M. L. Jouandet *et al.*, *J. Cog. Neurosci.* **1**, 88 (1989)], but these techniques are difficult to implement in regions where sulci run nearly parallel to slices, as they do in any slice plane through the occipital lobe.

18. Area VP has sometimes been labeled V3v (ventral V3), and area V4v has sometimes been labeled VA (ventroanterior area). More definitive statements of homology await future studies of the functional properties of these retinotopically defined regions in humans.

19. The gradients in retinal eccentricity and polar angle with respect to cortical *x* and *y*, ∇r and $\nabla \theta$, are vector quantities whose norms have units of degrees per millimeter (the reciprocal of the magnification factor). They were computed by fitting a plane to the *r* (or θ) values of the current vertex and its immediate neighbors with least squares. The clockwise angle, λ, between ∇r and $\nabla \theta$ was then measured to determine whether the local representation of the visual field at that vertex was non-mirror image (λ near $\pi/2$) or mirror image (λ near $-\pi/2$). Finally, the intensity of the field sign coloring at each point was scaled by the average significance of the eccentricity and polar angle data sets.

20. The limited resolution of the video projector made it difficult to present checkerboard patterns scaled with eccentricity near the center-of-gaze while still covering a reasonable amount of visual angle peripherally. Small imperfections in fixation also have a much more deleterious effect at the center-of-gaze than they do in the near periphery. In order not to occlude the fixation cross, the central 0.5° of the ring and semicircle stimuli were omitted. These considerations lead us to expect the periodic signal to fall off in the foveal parts of the visual field. This region of the visual field would be expected to be represented across several square centimeters of cortex just anterior to the occipital pole on the lateral surface of the brain. Mapping this region would require higher resolution stimuli and additional averaging to overcome fixation jitter.

21. D. C. Van Essen, C. H. Anderson, D. J. Felleman, *Science* **255**, 419 (1992).

22. J. D. Watson *et al.*, *Cereb. Cortex* **3**, 79 (1993); R. B. H. Tootell and J. B. Taylor, *ibid.* **5**, 39 (1995).

23. R. B. H. Tootell, M. S. Silverman, E. Switkes, R. L. De Valois, *Science* **218**, 902 (1982); D. C. Van Essen, W. T. Newsome, J. H. Maunsell, *Vision Res.* **24**, 429 (1984); D. J. Tolhurst and L. Ling, *Hum. Neurobiol.* **6**, 247 (1988); J. C. Horton and W. F. Hoyt, *Arch. Ophthalmol.* **109**, 816 (1991); E. L. Schwartz, in *Cerebral Cortex*, vol. 10, *Primary Visual Cortex in Primates*, A. Peters and K. S. Rockland, Eds. (Plenum, New York, 1994), pp. 359–411.

24. The falloff in the linear cortical magnification factor, *M* (millimeters of cortex per degree of visual angle), with increasing eccentricity has often been described with an equation of the form $M(r) = A[r + B]^{-C}$ (23), where *r* is the eccentricity and *A*, *B*, and *C* are constants (with *C* sometimes constrained to be 1). To estimate $M(r)$, we first marked activated regions (vertices) of the flattened visual field sign map by visual area and by whether they contained upper or lower field representations, omitting regions of ambiguous visual field sign. The average direction of the cortical eccentricity gradient (the vector sum of ∇r across every vertex assigned to an area) was estimated independently for each upper and lower visual field representation. The mapping function, $D(r) = \int M(r)dr$, where $D(r)$ is the distance in millimeters on the cortex from the center-of-gaze, was determined for each area by measuring distances from the most central response zone (representing approximately 0.5° eccentricity) along the direction of the average eccentricity gradient for each labeled vertex. The measurements were combined into 30 eccentricity bins. The resulting points were then fit with the equation for the mapping function

$$D(r) = \int M(r)dr = \frac{A(r + B)^{1-C}}{1 - C}, C \neq 1$$

by adjusting the parameters *A*, *B*, and *C*. The resulting cortical magnification factor equations for human

upper visual field V1, V2, VP, and V4 were $M_{V1}(r) = 20.05\,[r + 0.08]^{-1.26}$; $M_{V2}(r) = 25.19\,[r + 0.09]^{-1.53}$; $M_{VP}(r) = 18.28\,[r + 0.24]^{-1.75}$; and $M_{V4v}(r) = 18.17\,[r + 0.24]^{-1.55}$.

25. The magnification factor at a particular eccentricity will be proportional to the size of V1 if the shape of the mapping function (cortical distance versus eccentricity) does not change. To compare the mapping function for humans to that for owl monkeys (OM) and macaque monkeys (MM), we first scaled up the mapping functions for those animals to a human-sized V1 using values for *B* and *C* from the literature (23). The resulting equations for cortical magnification factor were $M_{OM}(r) = 19.83\,[r + 2.5]^{-1.0}$ and $M_{MM}(r) = 19.51\,[r + 0.94]^{-1.0}$.

26. Cortical magnification factor equations are sometimes constrained to have $C = 1$, which results in a particularly simple mapping function: $D(r) = A\log[r + B]$. This equation fits nonhuman primate data quite well. Our data could also be fit with this equation, but only if we allowed *B* to be negative, which results in a singularity (infinite magnification factor) before the center-of-gaze is reached. A good fit without a singularity could only be achieved with *C* above 1. The combinations of parameters given here fit the cortical distance data very closely but still give unrealistically large estimates of cortical magnification at the exact center of the fovea (extrapolation of the dotted portion of cortical magnification curve in Fig. 4C), indicating that the standard equation for *M* is inadequate to accurately describe cortical magnification in the very center of the fovea in humans even with $C > 1$. The data presented in (8) are consistent with ours in that $D(r)$ is almost vertical near the center-of-gaze; accurately fitting their cortical distance data at 2° to 10° eccentricity will give equally extreme estimates of cortical magnification at the exact center-of-gaze.

27. It is possible that differences at the level of the human retina (or lateral geniculate nucleus) may partly account for the differences in the cortical magnification factor we observed. For example, human OFF midget retinal ganglion cells have dendritic fields with diameters 70% those of their ON counterparts, a contrast not seen in the macaque monkey retina [D. M. Dacey, *J. Neurosci.* **13**, 5334 (1993)]; and the fibers of Henle are especially long in the human retina [C. A. Curcio and K. A. Allen, *J. Comp. Neurol.* **300**, 5 (1990)]. These observations are consistent with an increase in the foveal density of human midget ganglion cells with respect to macaque monkeys, which could explain our result.

28. S. E. Petersen, P. T. Fox, A. Z. Snyder, M. E. Raichle, *Science* **249**, 1041 (1990); A. C. Nobre, T. Allison, G. McCarthy, *Nature* **372**, 260 (1994).

29. We thank M. Kutas, R. Buxton, L. Anllo-Vento, and G. Ganis at University of California, San Diego (UCSD); T. Davis, J. Baker, C. Stern, R. Savoy, R. Benson, T. Campbell, and M. Vevea at the Massachusetts General Hospital Nuclear Magnetic Resonance Center; S. Engel, B. Wandell, and D. Rumelhart at Stanford University; T. DeYoe and E. Wong at Medical College of Wisconsin; J. Allman at California Institute of Technology; and D. Dacey at University of Washington for help, comments, and discussions. Supported by Office of Naval Research N00014-94-1-0856, the UCSD McDonnell-Pew Cognitive Neuroscience Center, the Norwegian Research Council, NIH grants MH47035, NICHD22614 (M. Kutas), EY07980, MH50054, HL39810, P01 CA48729, and by the Human Frontier Science Program.

9 January 1995; accepted 13 March 1995